Gas Atomization of Amorphous Aluminum: Part I. Thermal Behavior Calculations

BAOLONG ZHENG, YAOJUN LIN, YIZHANG ZHOU, and ENRIQUE J. LAVERNIA

In this article, the thermal history and cooling rate experienced by gas-atomized Al-based amorphous powders were studied via numerical simulations. Modeling simulations were based on the assumption of Newtonian cooling with forced convection, as well as an energy balance, which involves gas dynamics, droplet dynamics, and heat transfer between gas and droplet. To render the problem tractable, phase transformations, crystal nucleation, and growth were not taken into account in the analysis of the solidification of Al droplets; instead, an energy balance approach was formulated and used. The numerical results and associated analysis were used to optimize processing parameters during gas atomization of Al-based amorphous powder. The results showed that the cooling rate of droplets increases with decreasing powder size and can reach in excess of 10^5 K/s for powder <20 μm in diameter. Gas composition has a more significant influence on cooling rate than gas pressure, and 100 pct He has the highest cooling effect. The results also showed that the cooling rate increases with increasing melt superheat temperature.

DOI: 10.1007/s11663-009-9276-5

I. INTRODUCTION

THE unusual combination of engineering properties and potential critical structural and functional applications of metallic glasses (MGs) have attracted the interest of the scientific community. However, one of the biggest stumbling blocks of making the best use of MGs is their limited glass-forming ability (GFA), size, and cost, which represent challenges that are far from being adequately solved.[1,2] These factors have limited widespread adoption of MGs as structural materials in structural applications. Moreover, the high cooling rate that is required for the formation of MGs, the cost, and the limited available size have hindered the development of industrial processes for mass production of these unique materials.

High-strength and lightweight, cost-effective Al-based alloys are of interest in weight-critical applications. Accordingly, Al-based MGs, with their amorphous microstructure, exhibit unique combinations of mechanical properties, *e.g.*, strength, toughness, and corrosion resistance.[1,3,4] As a result of their low cost relative to that of conventional MGs with multicomponent chemistries, such as Zr-, La- and Pd-based MGs, and because of their potential use in various applications, Al-based MGs, such as $Al_{90}Gd_7Ni_2Fe_1$, were selected as the target materials to be investigated in the present study. One remarkable characteristic of most of this class of MGs is that the alloys contain >85 at pct of the base component Al.

MGs can be developed by cooling the melt fast enough to prevent detectable crystallization. The thermodynamic and kinetics of MG formation are related to controlling crystal nucleation and growth.[5] For Al-based MG formation, the required cooling rate is generally around 10^5 K/s,[1,4] and the possible rapid solidification processes to attain the required cooling rate include splat quenching,[6] twin-roller quenching,[7] melt spinning,[8] and gas atomization (GA).[9] Melt spinning and GA are most commonly used currently,[1] and melt spinning is popular for preparing specimens for scientific research because of easy process control. However, melt spinning is unlikely to evolve into a commercial process for large-scale engineering applications.[10] GA remains as an attractive approach and represents a promising route because it is suitable for large volume production.[1,11,12] Although the product of gas atomization is in powder form and is small in size, the amorphous powder can be further processed through various powder metallurgical techniques into engineering MG components.[12–15]

The thermal history experienced by atomized powder is one of the key factors that affect the initial formation and eventual retention of the amorphous phase. To maximize cooling rate, and thereby maximize the extent of amorphous fraction in atomized powders, controllable processing parameters that affect the cooling rate and the solidification process of atomized droplets require careful selection and control, particularly, if optimized GA is the goal. In addition, to understand the development of microstructure and properties in Al-based amorphous alloys, knowledge of the thermal history and cooling rate is required.

BAOLONG ZHENG and YAOJUN LIN, Post-Doctoral Researchers, YIZHANG ZHOU, Associate Researcher, and ENRIQUE J. LAVERNIA, Distinguished Professor, are with the Department of Chemical Engineering and Materials Science, University of California–Davis, Davis, CA 95616. Contact e-mail: bzheng@ucdavis.edu

Manuscript submitted November 18, 2008.
Article published online August 14, 2009.

During GA processing, powder experiences rapid solidification, which occurs under nonequilibrium conditions and is completed in a few milliseconds,[9] whereas the heat is extracted at high rates from the liquid mass via the smallest dimension. Recording temperature variations over such a short time and small scale is difficult. In particular, it is not possible to measure directly the temperatures and cooling rates of droplets during their residence in a high-velocity gas during GA. Accordingly, it is customary to estimate the cooling rate by numerical calculation of the droplet thermal histories during GA.

Numerical simulation is a powerful tool for solving these types of problems. The modeling results can be used to provide fundamental insight in support of the optimization of GA processing parameters. Inspection of the technical literature reveals some excellent research on numerical simulation of GA[16–19] and spray forming (SF),[20–22] which were principally concerned with relevant recalescence, crystal nucleation, and growth phenomena of conventional crystal alloys during GA or SF. A review of the scientific literature reveals that published numerical studies on the thermal behavior and process optimization of GA for metallic amorphous powders are essentially nonexistent. The fact that MGs generally have a higher melt viscosity than that of conventional alloys, and there is no obvious phase transformation, as well as no crystal nucleation and growth occurring during droplet solidification, suggest that such a study would be useful.

The primary technological goal of the work described herein is to provide insight into the thermal behavior of atomized Al MGs and to use this fundamental insight to optimize the processing parameters. This goal will be accomplished via a combination of numerical (part I of this study) and experimental (part II) studies. The scientific objective is to establish a fundamental understanding of the relationship between processing, thermal behavior, and microstructure evolution of amorphous Al powder during GA.

In this article, the thermal history and cooling rate experienced by gas-atomized Al-based amorphous powder were calculated based on the assumption of Newtonian cooling with forced convection. The rationale for the assumptions used was rationalized in light of available experimental data. The effects of processing parameters, such as gas composition, gas pressure, melt superheat temperature, and gas/melt flow ratios, on the thermal history and cooling rate were numerical simulated and analyzed. The complexities of the system studied required several simplifying assumptions as well as the use of empirical equations that will undoubtedly lead to discrepancies between theory and experimentation. Accordingly, experimental validation was deemed necessary and is reported in part II[23] of this study.

II. NUMERICAL FORMULATION

During the GA processing, a stream of molten metal is disintegrated into micron-sized droplets by the impact of high-energy gas jets.[9] The liquid breakup process depends on the relative velocity between the liquid and the atomization gas. Various breakup mechanisms have been proposed for the formation of droplets during GA, although experimental verification of these mechanisms remains limited.[9,24,25] It has been widely accepted that three basic stages are involved in the GA processing for the disintegration of an instable liquid sheet into droplets.[25]

Because of the initial high relative velocity between the droplets and the fast-moving cold gas stream during GA, elevated cooling rates can be produced with relatively high levels of undercooling. The cooling rates depend on the heat exchange between the atomized droplets and the surrounding medium via two types of heat transfer mechanisms: One is radiation toward the surrounding media and another is forced convection into the moving gas. In the case of Al and other low-melting-point metals, the latter is the predominant mechanism. The cooling rate of the droplets depends on several processing parameters, such as gas composition, gas pressure, melt superheat temperature, and gas/melt mass flow ratio.[9]

For the numerical simulations of thermal history and cooling rate experienced by the droplets, the calculations assume constant droplet acceleration and no overshoot between different thermal regions over a time step dt. In addition, it is assumed that Newtonian cooling occurs with forced convection and that no nucleation occurs before droplet temperature reaches the glass transition temperature T_g. Simplified assumptions are listed as follows: First, all droplets are spherical and formed instantaneously at the impact point with the gas stream, where the droplet velocity and flight distance is zero. Second, all droplets travel along the axis of the chamber, and subject the same gas velocity profile for all droplet sizes considered. Third, no interactions occur between droplets. Fourth, the fluctuation in the local gas velocity caused by turbulence is ignored, and only the mean gas flow is considered.

The primary modeling equations, including the energy balance, gas dynamics, droplet dynamics, properties of the alloy and atomization gas, and heat transfer between gas and droplet, are summarized below.

A. *Droplet Size Distribution*

The droplet size distribution for gas-atomized various alloys has been reported to follow a lognormal distribution.[21,26–29] The mass probability density function $p(d)$ of the droplet-size distribution can be expressed by[30–32]

$$p(d) = \frac{1}{\sqrt{2\pi}\ln\sigma_g}\exp\left[-\frac{(\ln d - \ln d_{50})^2}{2(\ln\sigma_g)^2}\right] \qquad [1]$$

where d is the droplet size. Generally, the powder size distribution is represented in terms of a cumulative frequency $f(d_i)$, which is defined as the fraction of powders that fall in the size range that is smaller than d_i. Another often used parameter for describing atomized power size is the mass median diameter d_{50}, which is defined as the droplet size that corresponds to the 50

pct cumulative frequency. d_{50} can be well predicted for gas atomizing Al alloys powder by using a correlation developed by Lubanska[27]:

$$d_{50} = K_d D_n \left[\frac{\eta_m}{\eta_g W} \left(1 + \frac{\dot{M}}{\dot{G}} \right) \right]^{\frac{1}{2}} \quad [2]$$

where K_d is a constant, D_n is the melt stream diameter (*i.e.*, the nozzle diameter); η_m (m^2/s) and η_g (m^2/s) are the kinematic viscosity of the melt and gas, respectively; $\dot{M}$ (kg/s) and $\dot{G}$ (kg/s) are the melt and gas flow rates, respectively; W is the Weber number; and $W = v_i^2 \rho_m D_n / \gamma_m$, where ρ_m (kg/m^3) and γ_m (J/m^2) are the density and surface tension of the melt, respectively.

σ_g is the geometric standard deviation characterizing the spread of the droplet size distribution centered around d_{50}, and it can be estimated by the following empirical equation[28,33]:

$$\sigma_g = q d_{50}^j \quad [3]$$

where q and j are constants and the unit of d_{50} is micrometer herein.

B. *Gas Dynamics*

1. *Gas initial velocity v_{g0}*

The dependence of gas velocity on gas pressure is a well-documented phenomenon that has been studied thoroughly in fluid mechanics. With Mach number M_a and sonic velocity v_s (m/s), the gas velocity at the nozzle exit (*i.e.*, initial velocity of atomization gas) v_{g0} (m/s) is given by[34]

$$v_{g0} = M_a v_s \quad [4]$$

In the case of the convergent–divergent atomizer used in the current investigation, compressible fluid mechanics, assuming steady state and isentropic flow for an ideal gas, give the following equation to calculate the Mach number (M_a) at the nozzle exit[35,36]:

$$M_a = C_M \left\{ \frac{2}{\gamma - 1} \left[\left(\frac{P_0}{P_e} \right)^{\frac{\gamma - 1}{\gamma}} - 1 \right] \right\}^{1/2} \quad [5]$$

where γ is the ratio of constant pressure to constant volume specific heat, C_M is a correlation coefficient used to take into account friction effects as well as the difference between the nozzle used and an ideal convergent-divergent one, P_0 (MPa) is the atomization gas pressure, and P_e (MPa) is the atomization gas pressure at the nozzle exit that approximates the chamber pressure.

The sonic velocity v_s (m/s) at the nozzle exit can be calculated by[37]

$$v_s = \left(\frac{\gamma R T_e}{m_{\text{mol}}} \right)^{1/2} \quad [6]$$

where m_{mol} (kg/mol) is the molar mass of the atomization gas and T_e (K) is the atomization gas temperature at the nozzle exit, which can be determined by the following equation[38]:

$$\frac{T_0}{T_e} = 1 + \frac{\gamma - 1}{2} M_a^2 \quad [7]$$

where T_0 (K) is the atomization gas temperature at the stagnation point (*i.e.*, atomization pressure).

2. *Decay equation of gas velocity*

Assuming the axial gas velocity decays exponentially with the axial flight distance, the relevant equation is given by[39]

$$v_g = v_{g0} \exp(-z/\lambda) \quad [8]$$

where v_g (m/s) is the axial gas velocity, z (m) is the flight distance, and λ is the gas velocity decay coefficient ($\lambda = 3.04 \times 10^{-4} v_{g0}^{1.24}$).

C. *Droplet Dynamics*

Following GA, each droplet is accelerated or decelerated because of the drag force that results from its velocity difference with the local atomization gas. The motion of an individual droplet along the spray-axis is governed by the following equation[40,41]:

$$\rho_d V_d \frac{dv_d}{dt} = V_d (\rho_d - \rho_g) g - \frac{1}{2} \rho_g A_s C_d |v_d - v_g| (v_d - v_g) \quad [9]$$

where v_d (m/s), ρ_d (kg/m^3), V_d (m^3), and A_s (m^2) are the velocity, density, volume, and cross-sectional area of a droplet, respectively; ρ_g (kg/m^3) and v_g (m/s) are the density and velocity of the GA gas; and g (m/s^2) is the gravitational acceleration, respectively. Because the gas-atomized droplets are treated as spherical in shape, $V_d = \frac{\pi}{6} d^3$ and $A_s = \frac{\pi}{4} d^2$, where d (m) is the effective droplet diameter. For a spherical droplet during GA, the drag coefficient, C_d, can be estimated by[42]

$$C_d = 0.28 + \frac{6\sqrt{\text{Re}} + 21}{\text{Re}} \quad [10]$$

where Re is Reynolds number determined by

$$\text{Re} = \frac{\rho_g d |v_g - v_d|}{\mu_g} \quad [11]$$

where μ_g (Ns/m^2) is the gas dynamic viscosity.

D. *Energy Balance Equations*

During GA, there is a large temperature difference between the molten metal droplets and the atomization gas. During droplet flight, heat extraction from the droplet surface occurs via radiative and convective cooling. In the range of typical droplet sizes and GA processing parameters, the heat conduction inside the droplets can be ignored, and homogenous temperature distribution within the droplet can be assumed with Newtonian cooling conditions and with forced

convection, because the magnitude of the Biot number, Bi, of droplets relative to the droplet/gas interfacial heat transfer is less than 0.1 and on the order of 10^{-3} to 10^{-2}.[9,43] The Biot number is a measure of the heat conduction in the liquid volume versus heat convection at the interface. For a droplet, Bi = $h_c \cdot d/2k_l$, where h_c is the heat transfer coefficient at the droplet/gas interface, and k_l is the thermal conductivity of the droplet. For small Bi values, the primary resistance to heat transfer occurs at the droplet/gas interface, and heat conduction within the droplet occurs relatively fast, resulting in small temperature gradients within the droplet. The temperature differential across the interior of the droplet can be safely neglected when Bi < 0.1.[43]

In view of the fact that our experiments involved a MG powder, we assumed that no nucleation occurs before the droplet temperature reaches the glass transition temperature T_g. The droplet cooling during the flight stage can be described by the following two consecutive processes: liquid-phase cooling and solid-phase cooling.

The energy conservation equation in a droplet is described by

$$-hA_d\left(T - T_{\text{gas}}\right) - A_d\varepsilon\sigma\left(T^4 - T_{\text{gas}}^4\right) = V_d\rho_d C_{pd}\frac{dT}{dt} \quad [12]$$

where T (K) is the droplet temperature, t (s) is time, T_{gas} (K) is the temperature of the ambient atomization gas, C_{pd} (Jkg^{-1} K^{-1}) is the melt specific heat, A_d (m^2) is the droplet surface area $A_d = \pi d^2$, ε is emissivity, σ is the Stephan-Boltzmann constant, (5.671×10^{-8} Wm^{-2} K^{-4}), ρ_d (kg/m^3) is the droplet density, and h (Wm^{-2} K^{-1}) is the convective heat transfer coefficient between a droplet and the atomization gas. This can be estimated by the following empirical equation[44,45]:

$$h = \frac{K_g}{d}\left(2 + 0.6\text{Re}^{\frac{1}{2}}\text{Pr}^{\frac{1}{3}}\right) \quad [13]$$

where K_g (Wm^{-1} K^{-1}) is the thermal conductivity of gas; Pr, the Prandtl number, is a nondimensional coefficient, and is given by[45]

$$\text{Pr} = \frac{\mu_g C_{pg}}{K_g} \quad [14]$$

where C_{pg} (Jkg^{-1} K^{-1}) is the gas specific heat.

Rewritten Eq. [13] is now as follows:

$$h = \frac{K_g}{d}\left(2 + 0.6\rho_g^{\frac{1}{2}}\left|v_g - v_d\right|^{\frac{1}{2}} \cdot C_{pg}^{\frac{1}{3}}\mu_g^{-\frac{1}{6}}K_g^{\frac{1}{3}}\right) \quad [15]$$

E. *Gas/Melt Flow Ratio*

The gas/melt flow ratio during GA was determined based on our experimental data, modeling results, and published research results[9] and described as follows:

For an ideal gas:

$$PV = nRT \quad [16]$$

The gas density: $\rho = W/V = nw/V \rightarrow n = \rho V/w$

$P = \rho RT/w$, when T is constant $\rho_1/\rho_2 = P_1/P_2$

So, $\rho_{\text{He}} = \rho_1 \ P_{\text{He}}/P_1 = 0.1624 \ P_{\text{He}}$ /0.101 MPa = 1.608 P_{He} kg/m^3

$\rho_{\text{N2}} = \rho_1 \ P_{\text{N2}}/P_1 = 1.12 \ P_{\text{N2}}$/0.101 MPa = 11.09 P_{N2} kg/m^3

When gas pressure is 6 MPa, according to Reference 9, the gas volume flow rate R_{N2}' = 0.065 m^3/s and R_{He}' = 0.175 m^3/s. The mass flow rate is as follows:

$$\begin{aligned} R_{\text{N2}} &= R_{\text{N2}}'\rho_{\text{N2}} = (0.065/6)\,P_{\text{N2}} \times 11.09P_{\text{N2}} \\ &= 0.12(P_{\text{N2}})^2(\text{kg/s}) \\ R_{\text{He}} &= R_{\text{He}}'\rho_{\text{He}} = (0.174/6)\,P_{\text{He}} \times 1.608P_{\text{He}} \\ &= 0.047(P_{\text{He}})^2(\text{kg/s}) \end{aligned}$$

When the mass flow rates of the two types of gas are the same, $R_{\text{N2}} = R_{\text{He}}$, and other conditions remain the same: $P_{\text{He}} = (0.12/0.047)^{1/2} \ P_{\text{N2}} = 1.6 \ P_{\text{N2}}$.

The melt mass flow rate was calculated from our actual experimental data; the weight of all the powder collected is 280 g, whereas the atomization time is 30 s.

The melt flow rate is as follows: $R_{\text{melt}} = 280/30 = 9.33$ g/s = 0.0093 kg/s

The He gas flow rate is as follows: $R_{\text{He}}'' = 0.047 \ P_{\text{He}}^2$ (P in MPa)

Gas/melt flow ratio = $0.047 \ P_{\text{He}}^2/0.0093 = 5.054 \ P_{\text{He}}^2$ (P in MPa)

Based on the above calculations, the influence of gas/melt flow ratio on cooling rate can be determined from the effects of gas pressure on the cooling rate. A nozzle diameter of 2.16 mm was used in our experiments, and because the melt flow rate increases with increasing nozzle diameter, this leads to a decrease in gas/melt flow ratio and a corresponding decrease in cooling rate.

F. *Properties of Atomization Gas and Model Alloy*

The $Al_{90}Gd_7Ni_2Fe_1$ (at pct) alloy is selected as the model material system, and He and Ar are selected as atomization gases. The properties of gas mixtures (ξ) can be estimated as a linear sum of the compositional gases, as follows:

$$\xi = f_{\text{He}}\xi_{\text{He}} + f_{\text{Ar}}\xi_{\text{Ar}} \quad [17]$$

where f_{He} and f_{Ar} are the volume percentage of He and Ar, respectively. ξ_{He} and ξ_{Ar} are the corresponding properties of He and Ar, respectively.

On the basis of the above equations, the Ar vol pct in the He-Ar gas mixture, which has a similar heat transfer coefficient to that of 50 pct He-50 pct N_2 (vol pct), can be estimated. As shown in the Table I, K_g and C_{pg} of He are much larger than those of N_2 and Ar. When 50 pct N_2 is replaced by 50 pct Ar in He-N_2 mixture, the change of K_g and C_{pg} can be safely neglected. However, μ_g and ρ_g increase slightly because of the higher exponent of ρ_g. To counteract the increase of ρ_g, the Ar vol pct should be slightly lower than 50 pct.

Most of the physical parameters used in the calculations are listed in Tables I and II. In fact, the physical

properties of the alloy do vary with temperature, but if the variation is not significant, then some of them can be approximately treated as a constant in the calculations.

The glass transition temperature T_g of Al-based alloys can be taken to be the crystallization temperature for α-Al in view of the fact that Al-based alloys do not reveal a T_g, and are marginal glass formers, so that for $Al_{90}Gd_7Ni_2Fe_1$ alloy, a glass transition temperature of 464 K is selected.[47]

The specific heat capacity, C_{pd} ($J \cdot mole^{-1} \cdot K^{-1}$), can be estimated for Al alloy from

$$C_{pd} = 21.8 + 0.009T \quad [18]$$

where T (K) is the droplet temperature. Because there is no phase transformation,[49] the difference of the specific heat between liquid and solid is neglected during the calculation of droplet thermal history.

The droplet viscosity μ_m (Ns/m^2) and its relationship with temperature can be calculated with Andrade's equation, as follows:

$$\mu_m V^{1/3} = A \exp(C/VT) \quad [19]$$

where V (m^3) is the specific volume, the volume occupied by a unit of mass of a material. It is equal to the inverse of density. T (K) is droplet temperature, the temperature-independent parameters $A = 2.353 \times 10^{-3}$ and $C = 581.2$.[50] The glass viscosity is strongly composition and temperature dependent. In fact, the viscosity of conventional Al alloys can be used to approximate that of the amorphous $Al_{90}Gd_7Ni_2Fe_1$ (at pct) alloy. This approximation is acceptable for the following reasons: (1) The concentration of the alloying elements is only 10 at pct, and (2) superheat used herein is higher than 623 K. Under such a high superheat, the viscosity of a marginal amorphous forming alloy with a fragile liquid behavior is comparable with that of a conventional crystallized alloy,[51] which is also supported by the experimental result that the morphology of the $Al_{90}Gd_7Ni_2Fe_1$ powder is spherical, as shown in part II.[23] In contrast, the morphology of powder that forms from alloys with a high melt viscosity and a strong liquid behavior is highly irregular.

Table I. Physical and Thermal Properties of He and Ar

Symbol	Values	Unit
$\eta_{g,\ Ar}$	1.4×10^{-4}	m^2/s
$\eta_{g,\ He}$	1.22×10^{-3}	m^2/s
$\eta_{g,\ mixture}$	$\eta_{g,\ mixture} = 1.4 \times 10^{-4}\ x_{Ar} + 1.22 \times 10^{-3}\ x_{He}$	m^2/s
$m_{mol,\ Ar}$	40	g/mol
$m_{mol,\ He}$	4	g/mol
$m_{mol,\ mixture}$	$m_{mol,\ mixture} = 40x_{Ar} + 4x_{He}$	g/mol
$\mu_{g,\ Ar}$	224.3	$10^{-6} \cdot Nsm^{-2}$
$\mu_{g,\ He}$	198.6	$10^{-6} \cdot Nsm^{-2}$
$K_{g,\ Ar}$	0.0179	$Wm^{-1}\ K^{-1}$
$K_{g,\ He}$	0.15015	$Wm^{-1}\ K^{-1}$
$C_{pg,\ Ar}$	520.67	$Jkg^{-1}\ K^{-1}$
$C_{pg,\ He}$	5278.0	$Jkg^{-1}\ K^{-1}$
$\rho_{g,\ Ar}$	1.5979	kgm^{-3}
$\rho_{g,\ He}$	0.1624	kgm^{-3}

Table II. Constant, Physical, and Thermal Properties of Alloy $Al_{90}Gd_7Ni_2Fe_1$ (at pct)

Symbol	Values	Unit	Reference
K_d	73	—	[46]
ρ_m	3545	kgm^{-3}	[47]
γ_m	$0.914\text{-}3.5 \times 10^{-4}(T\text{-}911)$	Jm^{-2}	[46]
q	0.517	—	[46]
j	0.316	—	[46]
C_M	0.2165	—	[46]
ε	0.035	—	[48]
T_g	464	K	[47]
T_m	916	K	[47]
T_0	300	K	

III. MODELING RESULTS AND ANALYSIS

The above-described numerical framework was used to calculate the dynamic and thermal behavior of the gas-atomized droplets with different processing parameters and the corresponding results are summarized in Figures 1 through 13.

A. *Dynamic of the Gas and Droplets*

Figure 1 shows the gas and droplet velocity change with gas pressure and flight time for a droplet of 20 μm in size. The gas velocity reaches a maximum at the exit of the atomizer nozzle, and it subsequently decreases with an approximately exponential decay as the flight distance increases. Because of the velocity difference between the droplets and the impinging gas stream during GA, the droplets are subjected to an accelerating drag force. The velocity of atomized droplets increases with increasing gas pressure.

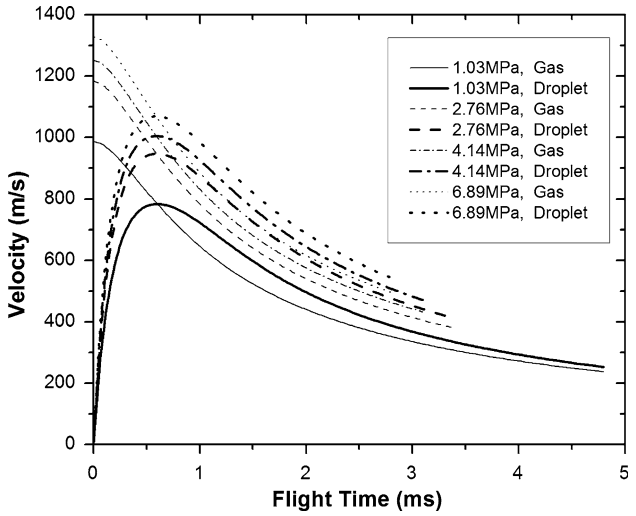

Fig. 1—Velocity variation of gas and droplets (20 μm) under different gas pressures.

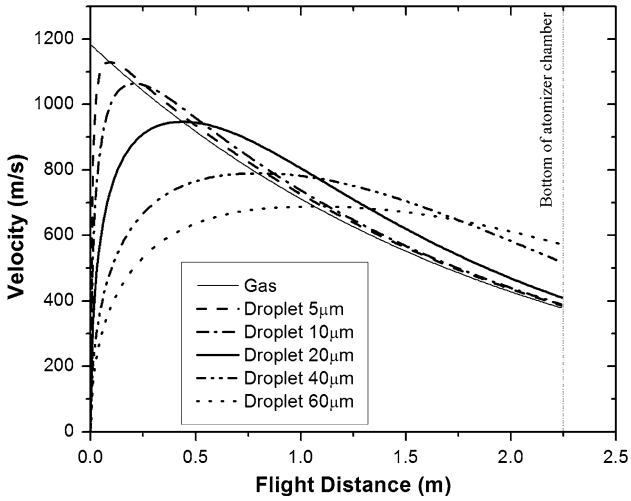

Fig. 2—Velocity variation of atomization gas and droplets with flight distance at a gas pressure of 2.76 MPa.

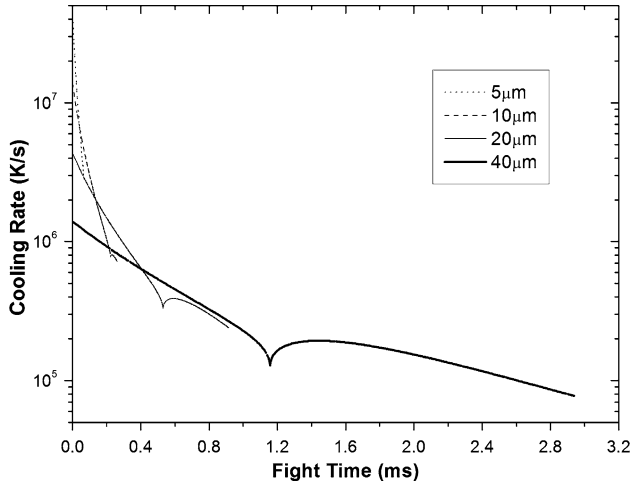

Fig. 3—Variation of droplet cooling rate during flight in gas atomization.

Figure 2 shows droplet velocity as a function of droplet size and flight distance for a gas pressure of 2.76 MPa. Initially, the droplets were rapidly accelerated to a maximum value (the gas velocity at that point) because of the gas drag force. The maximum velocity for 20 μm droplets is about 950 m/s at a flight distance of 0.5 m from the atomizer. Once the gas velocity has been exceeded, the velocity decreases monotonically because of the retarding drag force from the gas. Small diameter droplets (*e.g.*, 5 μm to 20 μm) are readily accelerated, whereas larger droplets (*e.g.*, >40 μm) have a larger inertia and hence resist the acceleration force.

B. *Thermal History of the Droplets*

The thermal behavior of the droplets is controlled by the processing conditions, such as the atomizing gas composition and pressure, gas/melt mass flow ratio, melt superheat temperature, and alloy composition. The heat removed by convection at a droplet's surface can be equated to the change in droplet temperature. As shown in Figure 3, the cooling rate decreases with increasing flight time during GA, and it also increases with decreasing droplet size. Both the maximum and the average cooling rate increase with decreasing droplet size.

Based on heat transfer considerations, the heat loss by forced convection is about two orders of magnitude greater than the loss by radiation.[17] To render the problem tractable, and neglecting radiation from Eq. [12], the cooling rate of the droplets can be estimated from

$$\dot{T} = \frac{6\left(T_{\text{melt}} - T_{\text{gas}}\right)h_i}{C_{pd}d} \qquad [20]$$

where

$$h_i = 2\frac{K}{d} + 0.6\left(\frac{u}{d}\right)^{\frac{1}{2}}\left(K^2 C_{pg}\right)^{\frac{1}{3}}\left(\frac{\rho_g}{\mu_g}\right)^{\frac{1}{6}} \qquad [21]$$

where u is the relative gas/droplet velocity.

From the above equations, it is apparent that cooling rate increases with increasing melt superheat temperature T_{melt} and decreasing gas temperature T_{gas}. Moreover, the cooling rate in the liquid state is proportional to $1/d^2$, which shows a strong dependence of cooling rate on powder size d and thermal conductivity K.

Equations [20] and [21] also show that a higher relative velocity will yield a higher cooling rate. As shown in Figure 3, the cooling rate decreases as droplets approach the gas velocity. The appearance of the local minimum points in the cooling curves is related to the change in droplet dynamics and corresponds to the point of the relative velocity of zero between the droplets and the gas as shown in Figure 2. At this point, the cooling rate falls instantaneously to a minimum value. Beyond this point, the cooling rate increases, as a differential velocity is reestablished.

C. *Effect of Processing Parameters on Cooling Rate*

1. *Gas Composition*

Figure 4 shows the influence of gas composition on the temperature profile for a 20-μm droplet, a gas pressure of 2.76 MPa, and a melt superheat temperature of 1373 K. It is evident that the temperature drops rapidly with increasing volume percentage of He in the atomization gas. This means that He is an efficient heat sink for rapid solidification and that the cooling efficiency of He is much higher than that of Ar. The droplet temperature decreases most efficiently when pure He used. In fact, because of He's relatively low molar (atomic) mass, both of its thermal conductivity and specific heat capacity are greater than any other gas except H_2. Therefore, pure He has highest cooling effect among all the gas compositions considered.

2. *Gas Pressure*

An increase in the atomization gas pressure can cause an increase in the cooling rate of the droplets because of

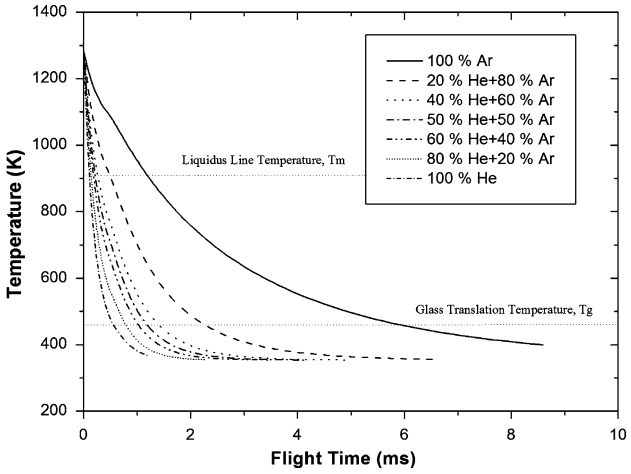

Fig. 4—Influence of gas composition on temperature variation of a 20-μm droplet.

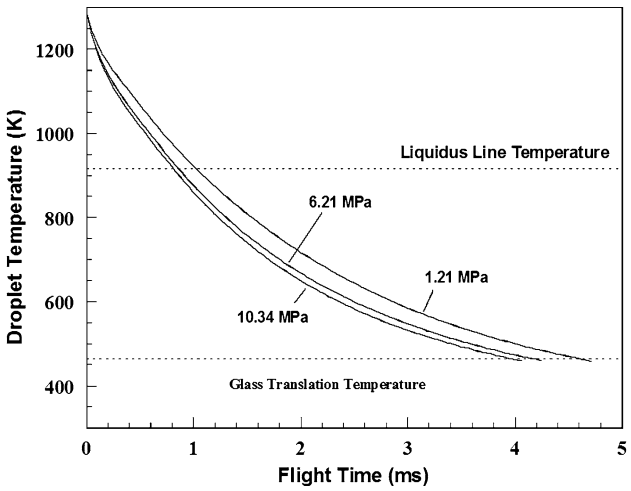

Fig. 5—Effects of gas pressure on temperature variation of a 20-μm droplet.

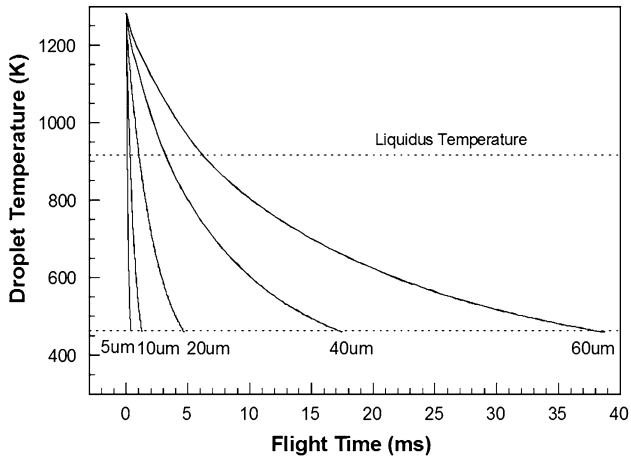

Fig. 6—Temperature variation as a function of droplet size.

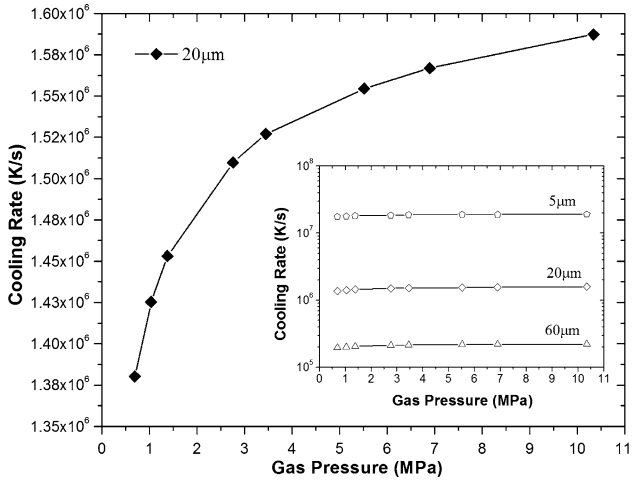

Fig. 7—Effect of gas pressure on cooling rate.

a shift of the droplet toward a smaller size distribution and higher gas/droplet relative velocities. Figure 5 shows that the influence of gas pressure of 100 pct He on the temperature profile of a 20-μm droplet (melt superheat temperature of 1373 K). When gas pressure increases from 1.21 to 10.34 MPa, the change in temperature is not evident for a specific size droplet, which suggests that the effect of gas pressure on cooling rate is not simple.

The effect of gas pressure on the cooling rate can be interpreted via changes in powder size, which in turn influences cooling rate. Figure 6 shows that droplet temperature decreases with decreasing powder size, which indicates that the cooling rate is a strong function of droplet size as shown in Figure 3. Figure 7 shows that the cooling rate increases with increasing gas pressure, and this trend is more apparent when gas pressure is under 2.76 MPa. The effects of gas pressure on the cooling rate of droplets with different sizes are shown in the inset in Figure 7. The results show a strong dependence of droplet size on cooling rate and a weak dependence of gas pressure.

Figure 8 shows that the cooling rate increases with increasing volume percentage of He in the gas composition. Using pure He gas can result in almost an order of magnitude improvement in the cooling rate for a given powder size. An analysis of the effect of atomization pressure indicates that pressure has a secondary influence on cooling rate. There is an apparent increase in cooling rate with increasing pressure in the low gas pressure range up to a certain value. Beyond this point, the cooling rate curve becomes flat, which suggests a weak dependence of cooling rate on gas pressure. Across a wide pressure range, the increase in cooling rate achieved is less than one order of magnitude. Comparing Figure 7 and Figure 8 shows that it is more efficient to increase cooling rate by increasing the He volume percentage relative than by increasing gas pressure.

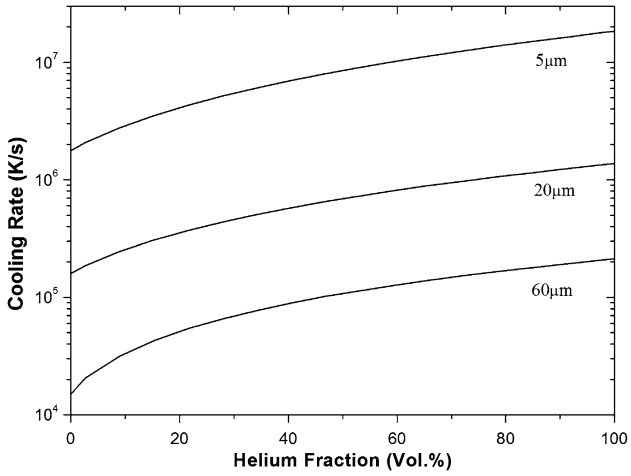

Fig. 8—Effect of gas composition on cooling rate for different size droplets.

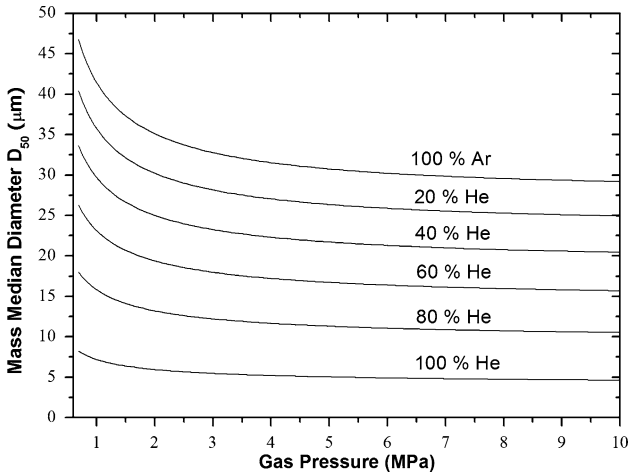

Fig. 9—Effect of gas pressure and composition on droplet size.

Figure 9 shows the effect of gas pressure and composition on droplet mass median size. The mass median diameter, d_{50}, decreases with increasing gas pressure, and it evidently decreases with increasing volume percentage of He. The effect of gas pressure on decreasing of droplet size is also apparent when gas pressure is under 2.76 MPa.

3. *Melt Superheat Temperature*

Melt superheat temperature has an influence on the thermal characteristics of the gas-atomized droplets. Figure 10 shows the influence of melt superheat temperature on the variation of cooling rate for a 20-μm droplet during GA with a gas composition of 100 pct He and a gas pressure of 2.76 MPa. It indicates that the cooling rate increases with increasing degree of melt superheat temperature. This may be readily rationalized if one considers that as melt superheat temperature is increased, the thermal gradient between melt and gas increases.

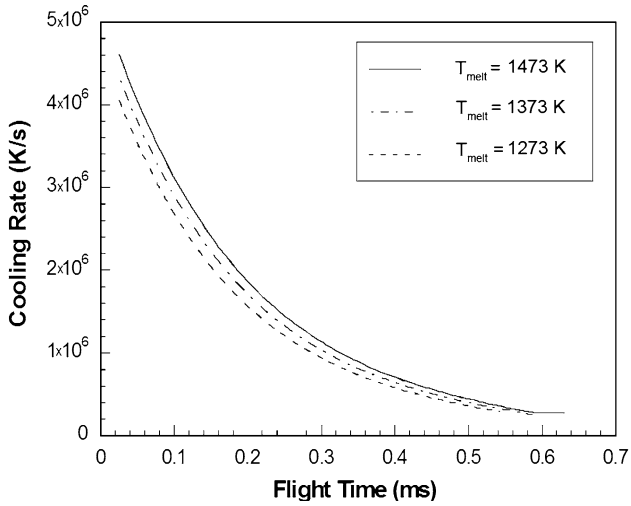

Fig. 10—Influence of melt superheat temperature on cooling rate for a 20-μm droplet.

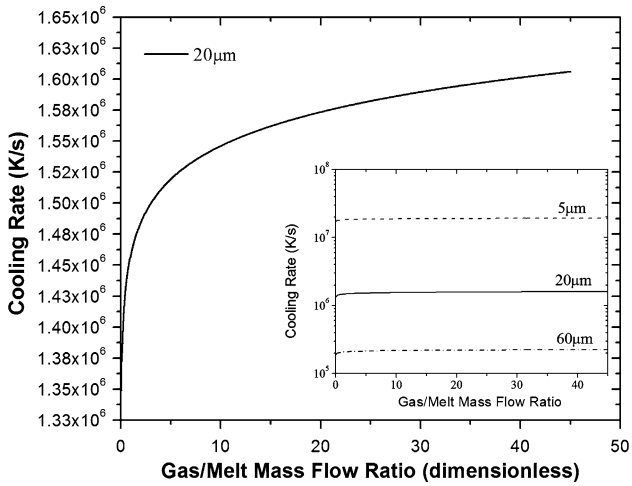

Fig. 11—Effects of gas/melt mass flow ratio on cooling rate for a 20-μm droplet.

In addition, experimental evidence suggests that increasing the melt superheat temperature significantly promotes a finer powder size distribution because of a decrease in melt density, melt surface tension, and viscosity.[9,17] Moreover, if the amount of melt superheat temperature is low, then there is a high probability that the metal will solidify in the delivery nozzle in the close-coupled confine atomizer, because of excessive heat removal caused by the atomizing gas.

4. *Gas/Melt Flow Ratio*

The influence of gas-to-melt mass flow ratio on the cooling rate of a 20-μm droplet is illustrated in Figure 11. The processing parameters used in this calculation correspond to the case of 100 pct He for the atomization gas, an atomizer that consists of 18 jets, and a nozzle diameter of 2.16 mm. The influence of gas/melt flow rate on cooling rate is similar to that

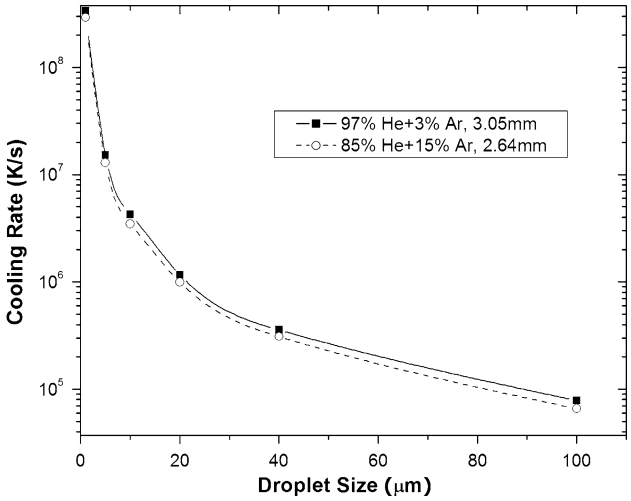

Fig. 12—Variation of cooling rate with droplet sizes for two sets of parameters.

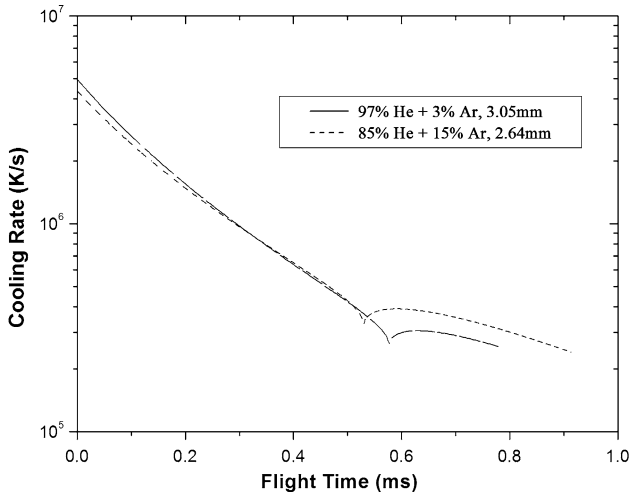

Fig. 13—Variation of cooling rate of a droplet with different gas compositions.

of gas pressure, for the same nozzle size. The cooling rate increases with increasing of gas/melt mass flow ratio for a specific droplet, and this effect is more apparent when the flow ratio is under about 5. Beyond this value, the curve becomes flat, which indicates that the influence of gas/melt flow ratio on cooling rate decreases rapidly with increasing flow ratio beyond the value of 5. The effects of gas/melt mass flow ratio on the cooling rate of droplets of various sizes are also illustrated in Figure 11.

5. *Influence of He vs Gas/Melt Flow Ratio*

Increasing the gas/melt flow ratio can be achieved by simply decreasing the nozzle orifice diameter. In practice, however, a smaller nozzle orifice can lead to premature metal solidification. In an effort to minimize the possibility of premature solidification in the nozzle as a result of the change in gas composition, the nozzle size is increased to 3.05 mm from 2.64 mm, and the gas composition is modified to 97 pct He + 3 pct Ar (vol pct) mixture gas from 85 pct He + 15 pct Ar. Figure 12 shows the calculation results of the average cooling rate with the two sets of parameters for different droplet sizes. The other processing parameters for both of the cases are same with a gas pressure of 2.76 MPa and a melt superheat temperature of 1100 °C. The comparison of the calculation results indicates that droplets experience a slightly higher mean cooling rate with 97 pct He + 3 pct Ar gas mixture and nozzle orifice diameter of 3.05 mm than that with 85 pct He + 15 pct Ar gas mixture and 2.64 mm of nozzle orifice diameter.

Figure 13 indicates that the cooling rate experienced by a 20-μm droplet with 97 pct He + 3 pct Ar gas mixture and 3.05 mm of nozzle orifice in size is slightly higher than that with 18 pct He + 15 pct Ar gas mixture and 2.64 mm nozzle during the initial period of the droplet flight. After that initial period, the cooling rate with 97 pct He + 3 pct Ar and 3.05 mm nozzle decreases and becomes slightly lower than that with 85 pct He + 15 pct Ar gas and 2.64 mm. Increasing the He volume percentage is more effective in terms of cooling rate during the initial period of the atomization; however, increasing gas/melt flow ratio is more effective after the atomization has started.

IV. DISCUSSION

The numerical results presented in last section demonstrate that there are two important factors that are necessary to attain a high cooling rate: gas composition and powder size. As the cooling media, gas composition has a significant influence on cooling rate. The influence of gas pressure on cooling rate is primarily to reduce the powder size and increase the relative velocity between gas and droplets. In fact, our experimental results in part II[23] show that the measured mean powder size is almost unchanged when gas pressure changes between 5.52 MPa and 2.62 MPa because of aspiration effects. For a specific nozzle diameter, the influence of gas/melt flow ratio on cooling rate is similar to that of the gas pressure results.

Numerical analysis provides useful insight into the thermal and momentum behavior of the atomized droplet dispersion, even if the size distribution of droplets is deduced from empirical data. For example, numerical modeling provided useful information regarding the complex interrelationships between the independent atomization parameters, such as atomization gas composition, gas pressure, melt superheat temperature, and gas/melt mass flow ratio, and their influence on the microstructure of solidification. Regarding the effects of He volume percentage in the atomizing gas, the results show that an increase in He content generally causes a decrease in powder size because of its low density which results in an increase in gas velocity, such as shown in Figure 9. However, the cooling effects of He gas on the melt viscosity also need to be considered for high viscosity materials. The high cooling capacity of He gas increases melt viscosity faster, as compared with N_2, Ar, and other gas mixtures. A rapid increase in viscosity

might have an adverse effect on the primary breakup of melt, as well as on the secondary breakup mechanisms. This might lead to an increase in the average powder size. In addition, an increase in the atomization gas pressure can generally cause a decrease in the powder size distribution. However, the presence of aspiration phenomena at the point of atomization can affect the melt flow rate and shift the droplet distribution toward a large size.[52] Such complex interactions, which are common in GA, make it difficult to accurately predict the overall cooling behavior of droplets. As a result, calculated cooling rates are often overestimated.

The numerical framework described in this article incorporates various empirical equations with several simplifying assumptions, such as physical parameters of the alloy, gas dynamics, and others, which may lead to some discrepancies between the real values of temperature or cooling rate and those obtained from numerical predictions. Therefore, an experimental validation of the calculated cooling rates is necessary and is described in part II of this study.[23] Experimental validation of the cooling rate experienced by the powders also shows that the cooling rate can reach more than 10^5 K/s order for powder size of <20 μm. The results of modeling calculation are consistent with the values of our experimental validation to a reasonable degree.

V. SUMMARY

In terms of the influence of processing parameters, the numerical results described in this article predict some trends, which are summarized below:

1. Gas composition is more effective than gas pressure on influencing cooling rate for a specific droplet size, and 100 pct He provides the highest cooling rate.
2. The cooling rates experienced by the atomized droplets increase with decreasing size, and the cooling rate can reach more than 10^5 K/s for a <20-μm powder.
3. Droplet size decreases with increasing gas pressure. The effect of increasing gas pressure on the cooling rate is marked when gas pressure is <2.76 MPa.
4. Gas/melt flow rate shows a similar effect to that of gas pressure on cooling rate when the nozzle orifice size is constant, and the cooling rate increases with increasing gas/melt mass flow ratio.
5. The cooling rate also increases with increasing melt superheat temperature. When the melt superheat temperature increases from 1373 K to 1473 K, the cooling rate can increase 7×10^4 K/s.
6. Based on the modeling results and analysis, the optimized processing parameters for GA of Al-based glass powder are atomization gas composition of 100 pct He, atomization pressure approximately 2.76 MPa, and melt superheat temperature of 1373 K.

ACKNOWLEDGMENTS

The authors thank the U.S. DARPA structural amorphous metals (SAM) program (Leading Institution: The Boeing Company) and the Materials Design Institute between Los Alamos National Laboratory and College of Engineering, University of California Davis, under Los Alamos National Laboratory contract number 25110-001-05, for financial support.

OPEN ACCESS

REFERENCES

1. A. Inoue: *Prog. Mater. Sci.*, 1998, vol. 43, pp. 365–520.
2. W.L. Johnson: *MRS Bull.*, 1999, vol. 24, pp. 42–56.
3. A. Inoue and H. Kimura: *Mater. Sci. Eng. A*, 2000, vol. 286, pp. 1–10.
4. S.K. Das, J.H. Perepezko, R.I. Wu, and G. Wilde: *Mater. Sci. Eng. A*, 2001, vols. 304–306, pp. 159–65.
5. M.C. Gao, R.E. Hackenberg, and G.J. Shiflet: *J. Alloys Compd.*, 2003, vol. 353, pp. 114–23.
6. E.W. Collings, A.J. Markworth, J.K. McCoy, and J.H. Saunders: *J. Mater. Sci.*, 1990, vol. 25, pp. 3677–81.
7. K.B.R. Varma: *Bull. Mater. Sci.*, 1987, vol. 9, pp. 1–5.
8. R.S. Tiwari, M.V. Heimendahl, and S. Ranganathan: *Z. Metallkde*, 1987, vol. 78, pp. 275–79.
9. E.J. Lavernia and Y. Wu: *Spray Atomization and Deposition*, John Wiley & Sons, New York, NY, 1996, pp. 95–99.
10. S.J. Hong and B. S. Chun: *Mater. Sci. Eng. A*, 2003, vol. 348, pp. 262–70.
11. Y.E. Kalay, L.S. Chumbley, and I.E. Anderson: *Materi. Sci. Eng. A*, 2008, vol. 490, pp. 72–80.
12. G. Xie, W. Zhang, D.V. Louzguine-Luzgin, H. Kimura, and A. Inoue: *Scripta Mater.*, 2006, vol. 55, pp. 687–90.
13. T.-S. Kim, J.-K. Lee, H.-J. Kim, and J.-C. Bae: *Mater. Sci. Eng. A*, 2005, vol. 402, pp. 228–33.
14. B. Zheng, Y. Zhou, J.E. Smugeresky, and E.J. Lavernia: *Metall. Mater. Trans. A*, 2009, vol. 40A, pp. 1235–45.
15. B. Zheng, Z. Zhang, T. Topping, Y. Zhou, C.Y.A. Tsao, and E.J. Lavernia: *TMS'09 Final Program,* San Francisico, CA, 2009, p. 41.
16. C.G. Levi and R. Mehrabian: *Metall. Mater. Trans. B*, 1980, vol. 11B, pp. 21–27.
17. T.W. Clyne, R.A. Ricks, and P.J. Goodhew: *Int. J. Rapid Solid.*, 1984, vol. 1, pp. 59–80.
18. H. Liu, H. Rangel, and E.J. Lavernia: *Acta Metall. Mater.*, 1994, vol. 42, pp. 3277–89.
19. C.G. Levi and R. Mehrabian: *Metall. Mater. Trans. A*, 1982, vol. 13A, pp. 221–34.
20. P. Mathur, D. Apelian, and A. Lawley: *Acta Metall. Mater.*, 1989, vol. 36, pp. 429–33.
21. P.S. Grant, B. Cantor, and L. Katgerman: *Acta Metall. Mater.*, 1993, vol. 41, pp. 3097–108.
22. W. Cai and E.J. Lavernia: *Metall. Mater. Trans. B*, 1998, vol. 29B, pp. 1085–91.
23. B. Zheng, Y. Lin, Y. Zhou, and E.J. Lavernia: *Metall. Mater. Trans. B*, 2009, in press.
24. S.D. Ridder, S.A. Osella, P.I. Espina, and F.S. Biancaniello: *Int. J. Powder Metall.*, 1992, vol. 28, pp. 133–47.
25. N. Dombrowski and W.R. Johns: *Chem. Eng. Sci.*, 1963, vol. 18, pp. 203–14.
26. X. Liang and E.J. Lavernia: *Mater. Sci. Eng. A*, 1993, vol. 161, pp. 221–35.
27. K. Lubanska: *JOM*, 1970, vol. 22, pp. 45–49.
28. E.J. Lavernia, T.S. Srivatsan, and R.H. Rangel: *J. Atom. Sprays*, 1992, vol. 2, pp. 253–74.

29. A. Unal: *Metall. Trans. B*, 1989, vol. 20B, pp. 61–69.
30. E.L. Crow and K. Shimizu: *Lognormal Distributions: Theory and Applications*, Marcel Dekker, New York, NY, 1988, pp. 2–6.
31. J.E. Smith and M.L. Jordan: *J. Colloid. Sci.*, 1964, vol. 19, pp. 549–59.
32. A.H. Lefebvre: *Atomizations and Spray*, Taylor & Francis, Bristol, PA, 1989, pp. 85–86.
33. A. Lawley: *Atomization: The Production of Metal Powders*, MPIF, Princeton, NJ, 1992, p. 74.
34. I.H. Shames: *Mechanics of Fluids*, 3rd ed., McGraw-Hill, New York, NY, 1992, pp. 312–13.
35. J. Szekely and N.J. Themelis: *Rate Phenomena in Process Metallurgy*, Wiley, New York, NY, 1971, p. 720.
36. D.R. Poirier and G.H. Geiger: *Transport Phenomena in Materials Processing*, TMS, Warrendale, PA, 1994, pp. 210–11.
37. J.E.A. John: *Gas Dynamics*, Allyn and Bacon, Boston, MA, 1969, p. 17.
38. R.W. Fox and A.T. McDonald: *Introduction to Fluid Mechanics*, Wiley, New York, NY, 1992, pp. 633–34.
39. P.S. Grant, B. Cantor, and L. Katgerman: *Acta Metall. Mater.*, 1993, vol. 41, pp. 3097–108.
40. W.E. Ranz and W.R. Marshall: *Chem. Eng. Prog.*, 1952, vol. 48, pp. 141–46.
41. Q.Q. Lu, J.R. Fontaine, and G. Aubertin: *Int. J. Heat Mass Transfer*, 1993, vol. 36, pp. 79–87.
42. R. Clift, J.R. Grace, and M.E. Weber: *Bubbles, Drops and Particles*, Academic Press, New York, NY, 1978, p. 111.
43. R. Mehrabian, S.C. Hsu, C.G. Levi, and S. Kou: *Advances in Metal Processing*, Plenum Press, New York, NY, 1981, p. 13.
44. F.H. Samuel: *Metall. Trans., A*, 1986, vol. 17A, pp. 73–91.
45. W.E. Ranz and W.R. Marshall: *Chem. Eng. Prog.*, 1952, vol. 48, pp. 141–46.
46. Y.J. Lin, Y. Zhou, and E.J. Lavernia: *Metall. Mater. Trans. B*, 2004, vol. 35B, pp. 1173–85.
47. L.F. Mondolfo: *Aluminum Alloys: Structure and Properties*, Butterworths, London, UK, 1976, p. 335.
48. Q. Xu, V.V. Gupta, and E.J. Lavernia: *Metall. Mater. Trans. B*, 1999, vol. 30B, pp. 527–39.
49. D.M. Bowden: *DARPA SAM Program*, 2002, pp. 1–21.
50. E. Rothwell: *J. Inst. Met.*, 1961/1962, vol. 90, pp. 389–94.
51. C.A. Angell: *Science*, 1995, vol. 267, pp. 1924–35.
52. J.S. Thompson: *J. Inst. Met.*, 1948, vol. 74, pp. 101–32.